Original Paper

Dynamic characteristics of the pipeline inspection gauge under girth weld excitation in submarine pipeline

Hang Zhang [a, *], Meng-Qi Gao [a], Biao Tang [b], Can Cui [a], Xue-Feng Xu [a]

[a] College of Mechanical and Storage and Transportation Engineering, China University of Petroleum-Beijing, Beijing, 102249, China
[b] CNPC offshore Engineering Co. Ltd, Beijing, 102200, China

ARTICLE INFO

ABSTRACT

Pipeline inner inspection technology based on Pipeline Inspection Gauge (PIG), is the primary means for ensuring the safety of submarine pipelines. The dynamic characteristics of a PIG can change abruptly with the excitation of obstacles such as girth welds inside the pipeline, which would result in failure or inaccuracy of the inspection results. This study establishes a dynamic model of the PIG sealing disc based on Kelvin spring damping in the circumferentially confined space. The axial vibration differential equations of the PIG is examined in detail. MSC/ADAMS is used to conduct the dynamic simulation of the PIG at different motion velocities and center of mass positions while passing through the girth weld process. Results indicate that the axial vibration caused by the girth weld intensifies substantially as the speed of the PIG increases, while the pitch and vertical vibrations exhibit a significant decline with an increase in the motion velocity. The change in the PIG's center of mass positions has little effect on its axial vibration, while the pitch and vertical vibration conditions are significantly different in the same circumstances.

1. Introduction

The transportation of offshore oil and gas are primarily achieved by using submarine pipelines. Long-term operation or the complexity of the maritime environment will cause defects in the submarine pipeline (Hu et al., 2014). Technology used for inspecting the interior of submarine pipelines is essential for the comprehensive testing and evaluation of submarine pipeline integrity. It refers to the online detection of corrosion, deformation, and cracks in pipelines by Pipeline Inspection Gauge (PIG), as shown in Fig. 1a. However, the accuracy of the test data regarding the pipe wall defects, the accuracy of the PIG mileage recording and positioning, as well as the reliability of the PIG during service are closely related to the stability of the PIG's motion (Yan et al., 2019; Quarini and Shire. 2007; Xie and Tian, 2018; Zhang et al., 2020; Shi et al., 2015; Zhao et al., 2013). As an important part of the PIG, the polyurethane sealing disc is in tight contact with the inner wall of the pipeline to induce a pressure difference in the medium contained within the pipeline to drive the PIG, as shown in Fig. 1b and

c. The dynamic contact between the polyurethane sealing disc and the pipe wall is one of the critical factors affecting the dynamic behavior of the PIG in the pipe, as shown in Fig. 1d. The frictional force between the sealing disc and the pipe wall, and external obstacles such as welds, can significantly affect the dynamic behavior of a moving PIG (Zhu et al., 2015; Yu et al., 2020). A girth weld that periodically appears in a length of pipeline can be considered as a periodic excitation for the moving PIG. The frequent axial vibration caused by the periodic girth weld excitation not only affects the accuracy of the internal inspection data but also causes vibration fatigue of the PIG structure (Fótos et al., 2012).

In 1964, McDonald et al. (Mcdonald and Baker, 1964) began to study the movement laws governing PIGs in multiphase flow pipelines. In recent years, Niechele et al. (Niechele et al., 2000; Esmaeilzadeh et al., 2009; Xu and Gong, 2005; Patricio et al., 2020) and other scholars used methods involving computational fluid dynamics to study the quasi-steady state, as well as the transient state of the PIG model movement. This process enabled them to obtain the motion law of the PIG driven by compressible gas. Therefore, it can predict pipeline operation parameters such as the operational velocity of PIGs, working time, and flow pattern. To improve the operation by dictating its movement within a stable

---

| List of symbols		R	Coordinate origin O to hinge point distance
		l	Rod length
k_1	Radial spring stiffness	θ	Angle between two adjacent rod
c_1	Radial damping coefficient	T	System kinetic energy
k_2	Circumferential spring stiffness	U	System potential
c_2	Circumferential damping coefficient	D	System energy dissipation function
k_3	Axial spring stiffness	M	System mass matrix
c_3	Axial damping coefficient	C	System damping matrix
α_i	No. i rod corner	K	System stiffness matrix
r_i	No. i mass block displacement	Q	System external load array
Q	System generalized coordinate array	M_O	PIG model center of mass
N	Number of mass block rod system	F	Driving force
M_i	No. i rod weight	F_f	Friction of the rod
m_i	No. i mass weight	R_w	Equivalent radius of the girth weld section
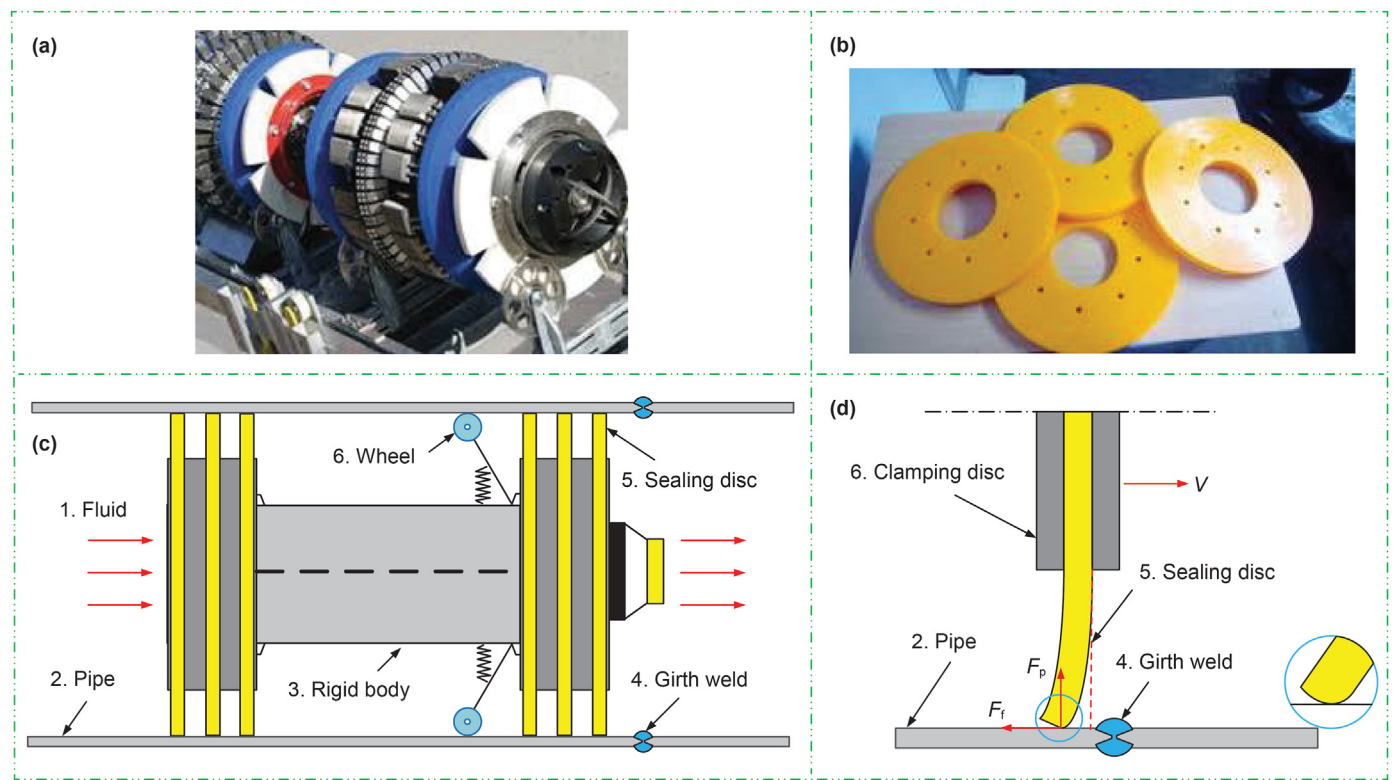
Fig. 1. a A typical PIG from the ROSEN Group; **b** Polyurethane sealing discs; **c** The basic structure of a PIG, as well as the pipe exhibiting a girth weld; **d** Deformation of the sealing disc by forcing it to pass through the girth weld.

velocity range, a PIG capable of adjusting velocity and including a bypass discharge device was designed (Liang et al., 2017). Nguyen et al., (2001; 2001; 2001) and his group systematic-ally studied the governing law of the damper valve velocity-adjusting PIG as well as the velocity characteristics of the velocity-adjusting PIG using the numerical simulation method. Hendrix et al., (2017) investigated the relationship between the motion of a PIG with a bypass and the pressure drop coefficient.

In addition to the study of the motion law of PIGs, the dynamics and ontology reliability of PIGs have also received attention. Aksenov et al. 2012, 2013 studied the self-oscillation problem of the PIG and established a dynamic model that can be used to optimize the structural parameters. Mirshamsi et al. (Mirshamsi and

Rafeeyan, 2012, 2015, 2015; Mirshamsi and Rafeeyan, 2015a,b) used numerical simulation to calculate the kinematic and dynamic response of the PIG under specific initial conditions. Podg-orbunskikh et al. (Hendrix et al., 2017; Tolmasquim and Nieckele, 2008) researched the design and test questions of PIGs to improve the stability of internal detection motion. Shi et al. (Shi et al., 2017; Ren et al., 2017) analyzed the possible reasons for the vibration of the PIG under liquid drive. The results indicate that the dynamic change in the contact force between the sealing disc and the pipe wall is primary cause of the vibration. Zhang et al., (2015, 2015) conducted a pulling test of different sized sealing discs to investigate the problem of colliding with the girth weld during the operation of the PIG. The results show that the PIG generates a

magnitude vibration response many times greater than that of the stable operation under the excitation of the girth weld.

Scholars have conducted extensive research on the motion model and motion law of PIGs and affirmed the importance of a stable operational state. However, the PIG is always regarded as a rigid object that will not be damaged. The methods employed for analysis are mostly experimental and simulative in nature, lacking theoretical model derivation and dynamic response research. This study proposes a dynamic model of the PIG sealing disc based on Kelvin spring damping, as well as a nonlinear dynamic model of the PIG system. Additionally, MSC/ADAMS is used to simulate the dynamic response of PIGs at different velocities and center of mass positions when they collide with the girth weld.

2. An equivalent multi-body dynamics model of a PIG sealing disc

An equivalent multi-body dynamics model of a PIG sealing disc is built based on Kelvin spring damping as shown in Fig. 2. The front view of the equivalent model referencing the sealing disc in the pipeline section is shown in Fig. 2a. The gray outer ring represents the pipe wall, while the central gray area denotes the body of the PIG. A continuum sealing disc is equivalent to a discrete system consisting of multiple groups of mass blocks and rigid rods. The sealing disc is affixed to the PIG body. Radial Kelvin spring damping connects the mass block and the fixed end of the sealing disc, and the stiffness damping coefficient is k_1, c_1. The mass block displays translational freedom only along the radial direction of the pipe. The thick green solid line indicates the rods, which are connected by the circumferential Kelvin spring damping, and the stiffness damping coefficient is k_2, c_2. The rod is hinged on the mass block with rotational freedom around the y-axis. Axial Kelvin spring damping connects the rod and the mass block, and the stiffness damping coefficient is k_3, c_3. Fig. 2b shows the left side view of the equivalent model of the sealing disc in the pipeline, and indicates the movement state of the mass block and rod system of the No. 1 and the No. i. The angle of the rod around the y-axis is α_1 and α_i, while the radial displacement of the mass block is r_1 and r_i. The front view denoting the movement state of the No. 1 and No. 2 mass block and rod system as it passes through the girth weld is represented by Fig. 2c. Fig. 2d shows the left side view representing the movement state of the No. 1 and No. 2 mass block and rod system as it passes through the girth weld.

The Lagrange equation allows for the theoretical model of the sealing disc to be established. A Cartesian coordinate system is created as shown in Fig. 2a, and the center of the PIG body denoted by O serves as the coordinate origin. The generalized coordinates are selected as the radial displacement of each mass block and represented by $r_1, r_2 \dots r_n$, the corner of each rod around the y-axis is $\alpha_1, \alpha_2 \dots \alpha_n$. The generalized coordinate array q can be expressed as $q = [r_1 \ r_2 \ \dots \ r_{n-1} \ r_n \ \alpha_1 \ \alpha_2 \ \dots \ \alpha_n \ \alpha_{n-1}]^T$, and the model exhibits $2n$ degrees of freedom.

Two groups of the mass block and rod systems of $n = 1$ and 2 are used as the research object. The mass of the rod is referenced by M_i, and the mass of the mass block is denoted by m_i. R refers to the distance from the origin of the coordinate O to the hinge point of the rod and mass block, while the length of the rod is represented by l. The angle between the 1 and 2 rods is θ. The arc length L corresponding to the angle θ is approximated to represent the original length of the circumferential spring. The first center of mass coordinates of rods 1 and 2 are signified by A and B. When the rod in the equivalent model of the sealing disc encounters the girth weld, the coordinates can be expressed as A' and B'. The length of the circumferential spring before and after the contact between the

equivalent model of the sealing disc and the girth weld can be calculated by:

$$|AB| = \sqrt{\left[\left(R + \frac{l}{2}\right)\theta\right]^2} = \left(R + \frac{l}{2}\right)\theta \tag{1}$$

$$|A'B'| = \sqrt{\left(\frac{l}{2}\alpha_2 - \frac{l}{2}\alpha_1\right)^2 + \left[\left(R + \frac{l}{2} - r_2\right)\theta\right]^2 + (r_1 - r_2)^2} \tag{2}$$

When the PIG passes through the girth weld, the compression and bending degree of each part of the sealing disc's circumferential direction are approximately equal. This is equivalent to a diameter reduction process, as shown in Fig. 2c and d, which means $\alpha_1 \approx \alpha_2, r_1 \approx r_2$, then:

$$|A'B'| \approx \sqrt{\left[\left(R + \frac{l}{2} - r_2\right)\theta\right]^2} = \left(R + \frac{l}{2} - r_2\right)\theta \tag{3}$$

The circumferential spring deformation between the 1 and 2 rods is:

$$\Delta L_1 = |A'B'| - |AB| = -r_2\theta \tag{4}$$

Since the system contains potential forces as well as non-potential forces. According to the Lagrangian theory, L is the Lagrangian expression, while Q_i is a generalized force corresponding to non-potential forces. Therefore, the Lagrange equation can be expressed as:

$$\frac{\mathrm{d}}{\mathrm{d}t}\left(\frac{\partial L}{\partial \dot{q}_i}\right) - \frac{\partial L}{\partial q_i} = Q_i \quad (i = 1, 2, \cdots, n) \tag{5}$$

The differential equation of motion for the system can be expressed in the following form by the kinetic energy T, the potential energy U, the system energy dissipation function D, and the generalized force Q_i corresponding to the generalized coordinate q_i:

$$\frac{\mathrm{d}}{\mathrm{d}t}\left(\frac{\partial T}{\partial \dot{q}_i}\right) - \frac{\partial T}{\partial q_i} + \frac{\partial U}{\partial q_i} + \frac{\partial D}{\partial \dot{q}_i} = Q_i \tag{6}$$
$$(i = 1, 2, \cdots, n)$$

The system kinetic energy is:

$$\begin{aligned} T = &\frac{1}{2}(m_1 + M_1)\dot{r}_1^2 + \frac{1}{2}(m_2 + M_2)\dot{r}_2^2 + \cdots + \frac{1}{2}(m_{n-1} + M_{n-1})\dot{r}_{n-1}^2 \\ &+ \frac{1}{2}(m_n + M_n)\dot{r}_n^2 \\ &+ \frac{1}{6}M_1 l^2 \dot{\alpha}_1^2 + \frac{1}{6}M_2 l^2 \dot{\alpha}_2^2 + \cdots + \frac{1}{6}M_{n-1} l^2 \dot{\alpha}_{n-1}^2 + \frac{1}{6}M_n l^2 \dot{\alpha}_n^2 \end{aligned} \tag{7}$$

The system potential energy is:

$$\begin{aligned} U = &\frac{1}{2}k_1 r_1^2 + \frac{1}{2}k_1 r_2^2 + \cdots + \frac{1}{2}k_1 r_{n-1}^2 + \frac{1}{2}k_1 r_n^2 + \frac{1}{2}k_2(-r_2\theta)^2 \\ &+ \frac{1}{2}k_2(-r_3\theta)^2 + \cdots \\ &+ \frac{1}{2}k_2(-r_n\theta)^2 + \frac{1}{2}k_2(-r_1\theta)^2 + \frac{1}{2}k_3\alpha_1^2 + \frac{1}{2}k_3\alpha_2^2 + \cdots + \frac{1}{2}k_3\alpha_{n-1}^2 \\ &+ \frac{1}{2}k_3\alpha_n^2 \end{aligned} \tag{8}$$

The system energy dissipation function is:

$$D = \frac{1}{2}c_1\dot{r}_1^2 + \frac{1}{2}c_1\dot{r}_2^2 + \cdots + \frac{1}{2}c_1\dot{r}_{n-1}^2 + \frac{1}{2}c_1\dot{r}_n^2 + \frac{1}{2}c_2(-\dot{r}_2\theta)^2$$
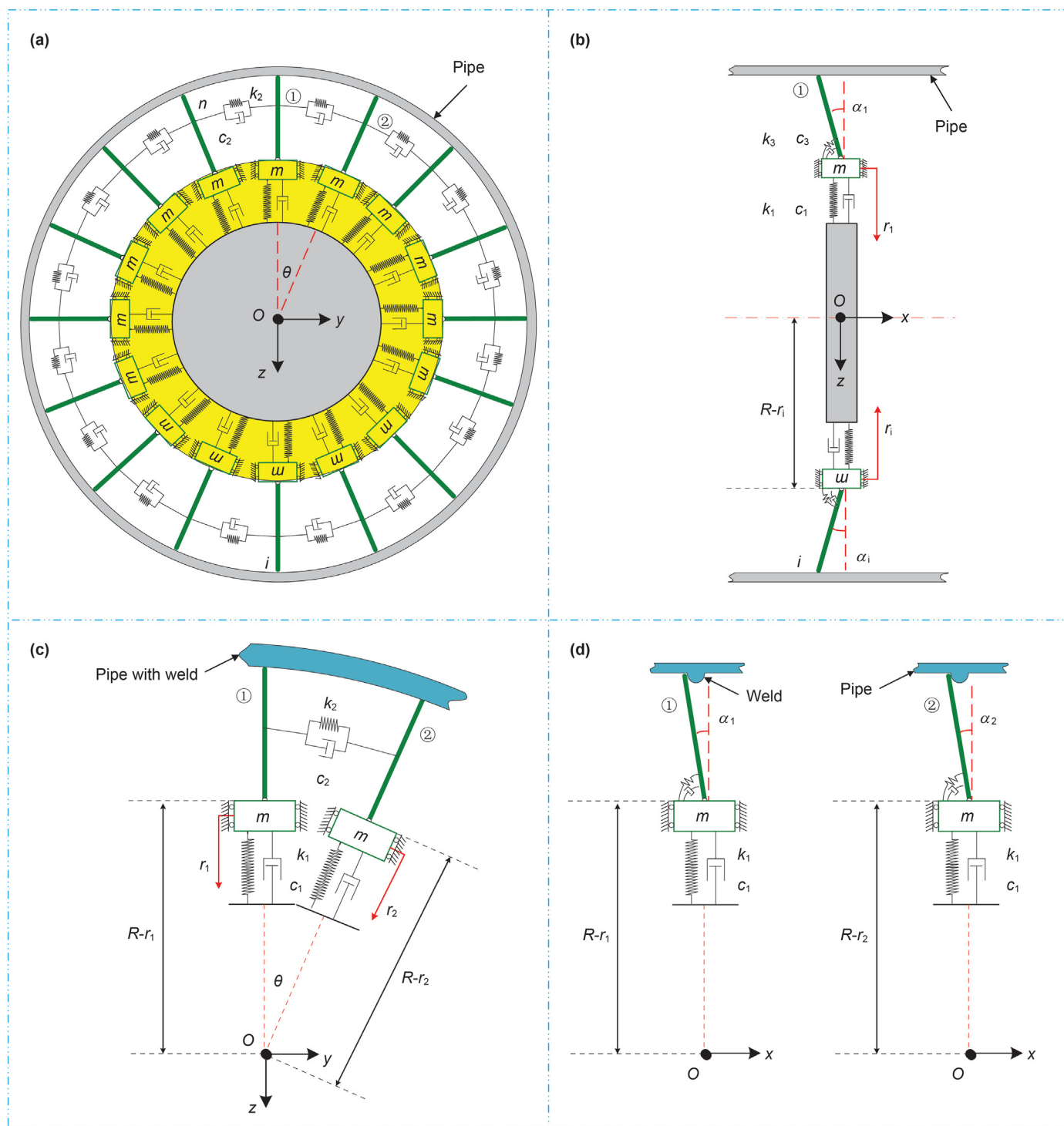
Fig. 2. The equivalent multi-body dynamics model of the sealing disc: **a** Front view and **b** Left side view of the sealing disc equivalent model; **c** Front view and **d** Left side view of the sealing disc partially passing through the girth weld.

$$+\frac{1}{2}c_2(-\dot{r}_3\theta)^2+\cdots$$

$$+\frac{1}{2}c_2(-\dot{r}_n\theta)^2+\frac{1}{2}c_2(-\dot{r}_1\theta)^2+\frac{1}{2}c_3\dot{\alpha}_1^2+\frac{1}{2}c_3\dot{\alpha}_2^2+\cdots+\frac{1}{2}c_3\dot{\alpha}_{n-1}^2$$

$$+\frac{1}{2}c_3\dot{\alpha}_n^2 \tag{9}$$

Substituting Eq. (6) to calculate the mass, damping, and stiffness matrix.

The mass matrix is: $\mathrm{M} = \begin{bmatrix} A & \\ & B \end{bmatrix}$

$$A = \begin{bmatrix} M_1 + m_1 & & & & \\ & M_2 + m_2 & & & \\ & & \ddots & & \\ & & & M_{n-1} + m_{n-1} & \\ & & & & M_n + m_n \end{bmatrix} \tag{10}$$

$$B = \begin{bmatrix} \frac{1}{3}M_1 l^2 & & & & \\ & \frac{1}{3}M_2 l^2 & & & \\ & & \ddots & & \\ & & & \frac{1}{3}M_{n-1} l^2 & \\ & & & & \frac{1}{3}M_n l^2 \end{bmatrix} \tag{11}$$

The damping matrix is: $C = \begin{bmatrix} D & \\ & E \end{bmatrix}$

$$D = \begin{bmatrix} c_1 + c_2 \theta^2 & & & \\ & c_1 + c_2 \theta^2 & & \\ & & \ddots & \\ & & & c_1 + c_2 \theta^2 \\ & & & & c_1 + c_2 \theta^2 \end{bmatrix} \tag{12}$$

$$E = \begin{bmatrix} c_3 & & & \\ & c_3 & & \\ & & \ddots & \\ & & & c_3 \\ & & & & c_3 \end{bmatrix} \tag{13}$$

The stiffness matrix is: $K = \begin{bmatrix} F & \\ & G \end{bmatrix}$

$$F = \begin{bmatrix} k_1 + k_2 \theta^2 & & & \\ & k_1 + k_2 \theta^2 & & \\ & & \ddots & \\ & & & k_1 + k_2 \theta^2 \\ & & & & k_1 + k_2 \theta^2 \end{bmatrix} \tag{14}$$

$$G = \begin{bmatrix} k_3 & & & \\ & k_3 & & \\ & & \ddots & \\ & & & k_3 \\ & & & & k_3 \end{bmatrix} \tag{15}$$

Each of the sub-matrices above is a $n \times n$ square matrix, and the differential equation of motion for the system can be expressed as:

$$M\ddot{q} + C\dot{q} + Kq = Q \tag{16}$$

3. The dynamics model of a PIG with two sealing discs

The multi-body dynamics model shown in Fig. 3a can be used to analyze the axial dynamic characteristics of the PIG. The model's center of mass is located at the M_O point, and the distance from the center of mass to the front and back of the model is L_1 and L_2. F_f indicates the friction of each rod, and the driving force F acts on the center of mass. In this two-dimensional symmetric model, the generalized coordinates are selected as rigid body axial displacement x, mass block displacement r_1, r_2, r_3, r_4, rod rotation angle α_1, α_2, α_3, α_4.

(1) When the radial spring stiffness is significantly less than the axial spring stiffness, the integral model only compresses the radial spring as it passes through the girth weld, as shown in Fig. 3b.

As illustrated by Fig. 3b, when the integral model has x displacement in the axial direction, the corresponding radial spring deformation is:

$$\Delta l = \sqrt{R_w^2 - (R_w - x)^2} \tag{17}$$

The system kinetic energy is:

$$T = \frac{1}{2}M\dot{x}^2 + \frac{1}{2}(M_1 + m_1)\dot{r}_1^2 + \frac{1}{2}(M_2 + m_2)\dot{r}_2^2 + \frac{1}{2}(M_3 + m_3)\dot{r}_3^2 + \frac{1}{2}(M_4 + m_4)\dot{r}_4^2 \tag{18}$$

The system potential energy is:

$$U = \frac{1}{2}k_1 \left(\sqrt{R^2 - (R - x)^2} + r_1 \right)^2 + \frac{1}{2}k_1 \left(\sqrt{R^2 - (R - x)^2} + r_2 \right)^2 + \frac{1}{2}k_1 r_3^2 + \frac{1}{2}k_1 r_4^2 \tag{19}$$

The energy dissipation function of the system is:

$$D = \frac{1}{2}c_1 \left[\left(R^2 - (R - x)^2 \right)^{-\frac{1}{2}} (R - x)\dot{x} + \dot{r}_1 \right]^2 + \frac{1}{2}c_1 \left[\left(R^2 - (R - x)^2 \right)^{-\frac{1}{2}} (R - x)\dot{x} + \dot{r}_2 \right]^2 + \frac{1}{2}c_1 \dot{r}_3^2 + \frac{1}{2}c_1 \dot{r}_4^2 \tag{20}$$

Substituting Eq. (6) to calculate the integral model axial vibration differential equation:

$$M\ddot{x} - k_1 \left(\sqrt{R^2 - (R - x)^2} + r_1 \right) \frac{(R - x)}{\sqrt{R^2 - (R - x)^2}} - k_1 \left(\sqrt{R^2 - (R - x)^2} + r_2 \right) \cdot \frac{(R - x)}{\sqrt{R^2 - (R - x)^2}}$$

$$+ c_1 \left[\frac{(R - x)}{\sqrt{R^2 - (R - x)^2}} \dot{x} + \dot{r}_1 \right] \frac{(R - x)}{\sqrt{R^2 - (R - x)^2}} + c_2 \left[\frac{(R - x)}{\sqrt{R^2 - (R - x)^2}} \dot{x} + \dot{r}_2 \right] \frac{(R - x)}{\sqrt{R^2 - (R - x)^2}} = F \tag{21}$$
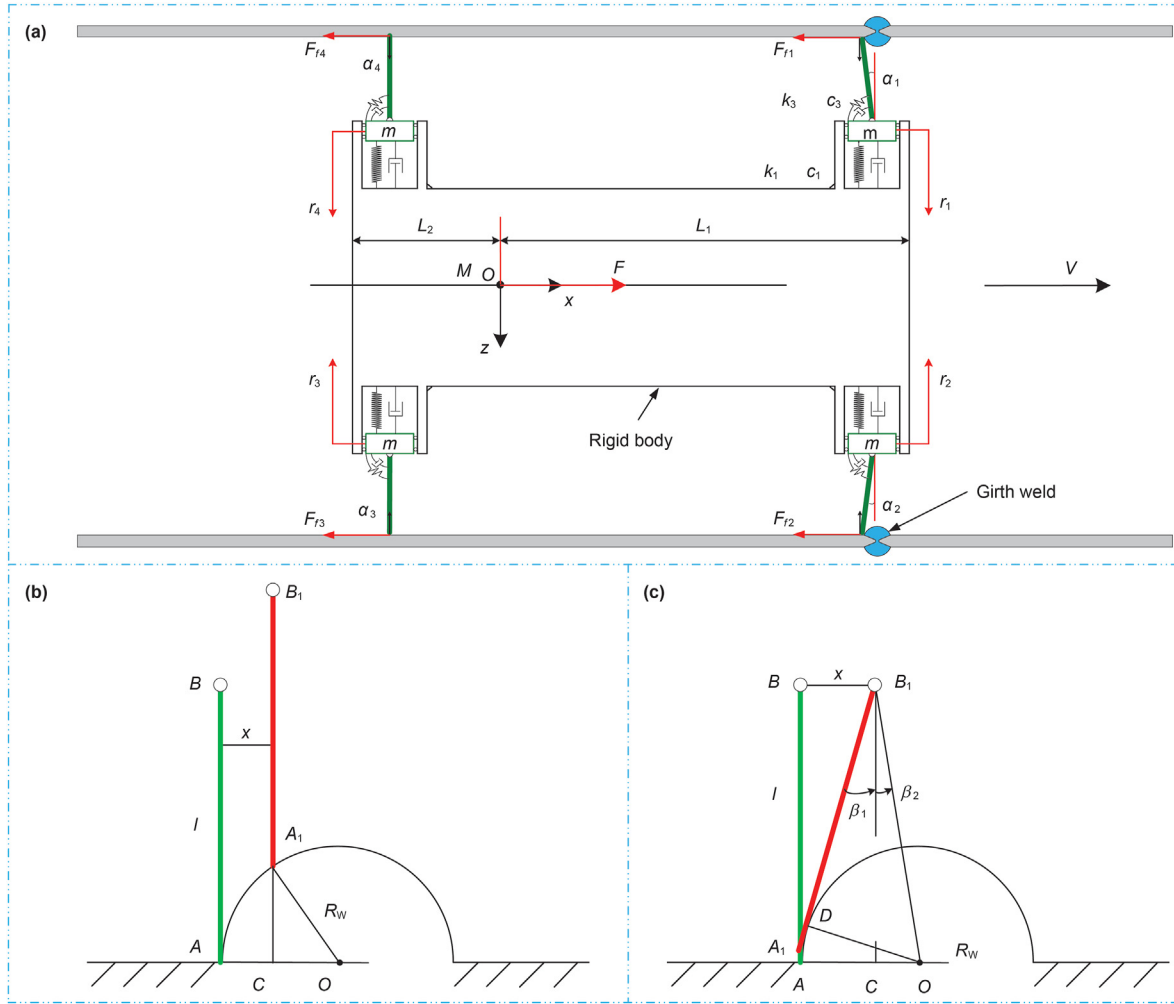
Fig. 3. a Schematic diagram of the axial movement of the integral model; **b** Rod without deflection and only radial compression; **c** Rod with deflection only and no radial compression.

$$(M_1 + m_1)\ddot{r}_1 + c_1\left[\left(\frac{(R - x)}{\sqrt{R^2 - (R - x)^2}}\dot{x} + \dot{r}_1\right)\right.$$

$$\left.\times\right] + k_1\left(\sqrt{R^2 - (R - x)^2} + r_1\right) = F_{f1} \qquad (22)$$

$$(M_2 + m_2)\ddot{r}_2 + c_1\left[\left(\frac{(R - x)}{\sqrt{R^2 - (R - x)^2}}\dot{x} + \dot{r}_2\right)\right.$$

$$\left.\times\right] + k_1\left(\sqrt{R^2 - (R - x)^2} + r_2\right) = F_{f2} \qquad (23)$$

$$(M_3 + m_3)\ddot{r}_3 + c_1\dot{r}_3 + k_1 r_3 = F_{f3} \qquad (24)$$

$$(M_4 + m_4)\ddot{r}_4 + c_1\dot{r}_4 + k_1 r_4 = F_{f4} \qquad (25)$$

(2) When the radial spring stiffness substantially exceeds the axial spring stiffness, the integral model only passes through the girth by the rotation of the rod, as shown in Fig. 3c.

Fig. 3c indicates that when the integral model has x displacement in the axial direction, the corresponding rod rotation angle β is:

$$\beta = \arcsin\left(\frac{R_w}{l}\cos\left(\arctan\frac{R_w - x}{l}\right)\right) - \arctan\frac{R_w - x}{l} \qquad (26)$$

The system kinetic energy is:

$$T = \frac{1}{2}M\dot{x}^2 + \frac{1}{6}M_1 l^2\dot{\alpha}_1^2 + \frac{1}{6}M_2 l^2\dot{\alpha}_2^2 + \frac{1}{6}M_3 l^2\dot{\alpha}_3^2 + \frac{1}{6}M_4 l^2\dot{\alpha}_4^2 \qquad (27)$$

The system potential energy is:

$$U = \frac{1}{2}k_3(\alpha_1 - \beta)^2 + \frac{1}{2}k_3(\alpha_2 - \beta)^2 + \frac{1}{2}k_3\alpha_3^2 + \frac{1}{2}k_3\alpha_4^2 \qquad (28)$$

The energy dissipation function of the system is:

$$D = \frac{1}{2}c_3(\dot{\alpha}_1 - \dot{\beta})^2 + \frac{1}{2}c_3(\dot{\alpha}_2 - \dot{\beta})^2 + \frac{1}{2}c_3\dot{\alpha}_3^2 + \frac{1}{2}c_3\dot{\alpha}_4^2 \qquad (29)$$

Substituting Eq. (6) to calculate the integral model axial

vibration differential equation:

$$M\ddot{x} + c_3(\dot{\alpha}_1 - \dot{\beta})\frac{\partial(-\dot{\beta})}{\partial \dot{x}} + c_3(\dot{\alpha}_2 - \dot{\beta})\frac{\partial(-\dot{\beta})}{\partial \dot{x}} + k_3(\alpha_1 - \beta)\frac{\partial(-\beta)}{\partial x}$$

$$+ k_3(\alpha_2 - \beta)\frac{\partial(-\beta)}{\partial x} = F \tag{30}$$

$$\frac{1}{3}M_1 l^2 \ddot{\alpha}_1 + c_3(\dot{\alpha}_1 - \dot{\beta}) + k_3(\alpha_1 - \beta) = F_{f1} \tag{31}$$

$$\frac{1}{3}M_2 l^2 \ddot{\alpha}_2 + c_3(\dot{\alpha}_2 - \dot{\beta}) + k_3(\alpha_2 - \beta) = F_{f2} \tag{32}$$

$$\frac{1}{3}M_3 l^2 \ddot{\alpha}_3 + c_3\dot{\alpha}_3 + k_3\alpha_3 = F_{f3} \tag{33}$$

$$\frac{1}{3}M_4 l^2 \ddot{\alpha}_4 + c_3\dot{\alpha}_4 + k_3\alpha_4 = F_{f4} \tag{34}$$

Table 1
Main parameters of the ADAMS simulation model.

| Model material	Steel
Pipe inner diameter	150, mm
Girth weld height	2, mm
Girth weld length	10, mm
Center of mass position	(0, 0, 0)
Model length	200, mm
Model mass	3.14, kg
Model for x-axis moment of inertia	9496.21, mm^4
Model for y-axis moment of inertia	9496.21, mm^4
Model for z-axis moment of inertia	3614.14, mm^4
Radial spring stiffness	50, N/mm
Radial spring damping	0.01, N·s/mm
Axial spring stiffness	20, N·mm/deg
Axial spring damping	0.01, N·s/deg
Circumferential spring stiffness	50, N/mm
Circumferential spring damping	0.01, N·s/mm
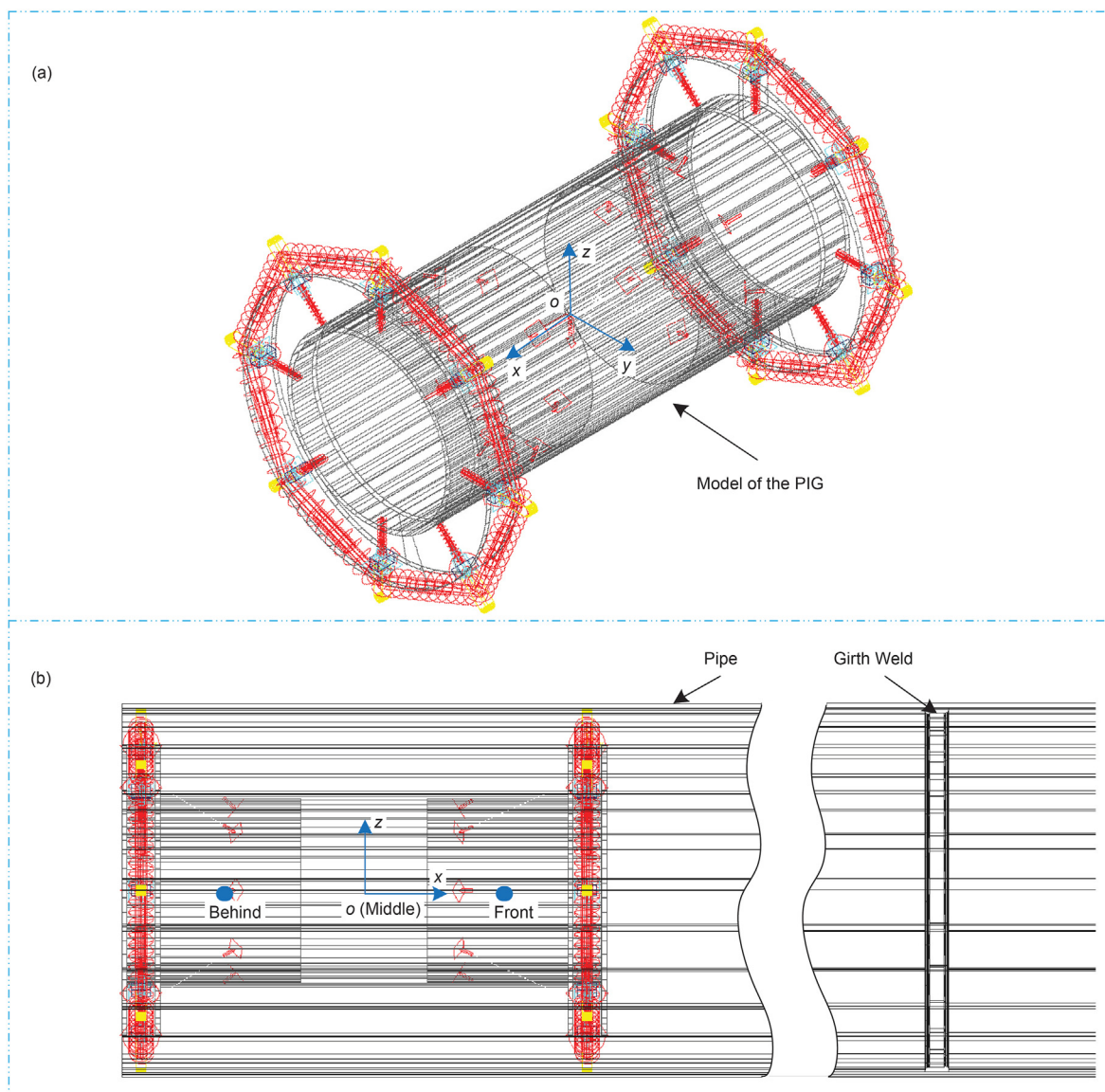
Fig. 4. a PIG model in ADAMS; **b** PIG model and the pipe system containing the girth weld.

Table 2
The first eight modes of the ADAMS simulation model.

Modes order	First order	Second order	Third order	Fourth order
Frequency, Hz	1.84×10^{-13}	5.34×10^{-8}	2.75	38.55
Modes order	Fifth order	Sixth order	Seventh order	Eighth order
Frequency, Hz	40.77	63.55	67.25	470.16

4. Dynamics simulation

4.1. Dynamic model

Based on the established theoretical model, the PIG simulation model was built using MSC/ADAMS dynamics analysis software. As shown in Fig. 4a, the simulation model includes the front and rear sealing disc models, each of which is composed of eight mass block and rod systems. This PIG model has 38 degrees of freedom, and each rod has a degree of rotation freedom around its respective rotating pair. Each mass block has translational freedom along the sliding pair while the PIG body has both translational and rotational degrees of freedom along three axes of the global coordinate system. The main design parameters of the model are shown in Table 1, and the first eight modes of the model obtained from ADAMS are shown in Table 2. At the initial moment, the PIG is located on the left side of the horizontal pipe section of the fixed pipe, and the girth weld is located in the middle of the pipe as shown in Fig. 4b. The rod and the inner wall of the pipe are making solid-to-solid contact, the static friction coefficient is 0.3, and the dynamic friction coefficient is 0.25.

4.2. Simulation process

The driving force shown in Fig. 5a is applied to the center of the PIG. When the sealing disc model does not encounter the girth weld, the driving force is equal to the friction of the PIG model. Two triangular pulses are evident upon contact between the front and rear sealing disc model and the girth weld. The amplitude spectrum of the driving force is shown in Fig. 5b, the first peak frequency is 7.9 Hz, while the rest represents the higher harmonic component of this frequency.

The simulation time was set to 1 s and 250 calculation steps. Table 3 lists the three integration methods of the ADAMS

simulation software. Since the SI2 integral format considers the velocity constraint equation, the accuracy of the calculated velocity and acceleration is improved. Therefore, the SI2 integration format is chosen for this study.

Table 4 lists three rigid stabilization algorithms that are commonly used. The Wstiff solver uses the NDF (Newton Divided Difference) formula in the estimation. The step information is used to modify the coefficient of the corresponding order, while accuracy remains unaffected by the step change. Therefore, the Wstiff solver is chosen.

The operating velocity of a PIG is an essential process parameter for pipe pigging and internal inspection operation. To study the dynamic response of a PIG when it collides with the girth weld at different motion velocities, three sets of velocities of 1.5 m/s, 2.5 m/s and 3.5 m/s were selected, while the PIG's center of mass is located in the front, middle and rear the three different positions. The response of the axial, vertical and pitch accelerations of the PIG was solved using MSC/ADAMS simulation software.

5. Simulation result and discussion

5.1. Dynamic response of the PIG at different motion velocities

（1）Dynamic response in the axial direction of the pipeline

Fig. 6a illustrates the time history curve indicating the PIG's center of mass along the x-axis at a motion velocity of 1.5 m/s. Two significant changes in pulse amplitude are evident, which are caused by the front and rear sealing discs passing through the girth weld. When the edge of the sealing disc passes over the highest point of the girth weld and bounces off it, the PIG acceleration reaches its maximum level, while the minimum degree of acceleration occurs during the deceleration of the PIG after contact with the girth weld. Compared with the smooth motion process of the initial state, when the PIG passes over the girth weld, noticeable collision vibration will occur. The amplitude spectrum of the PIG's center of mass along the x-axis at a motion velocity of 1.5 m/s is shown in Fig. 6b. It appears that the vibration amplitude is mainly concentrated in the range of 0−200 Hz. The fundamental frequency is 9.4 Hz, the highest amplitude in the figure is 0.25 g, and the peak frequency is 75.6 Hz. The power spectrum of the PIG's center of mass along the x-axis at a motion velocity of 1.5 m/s is shown in
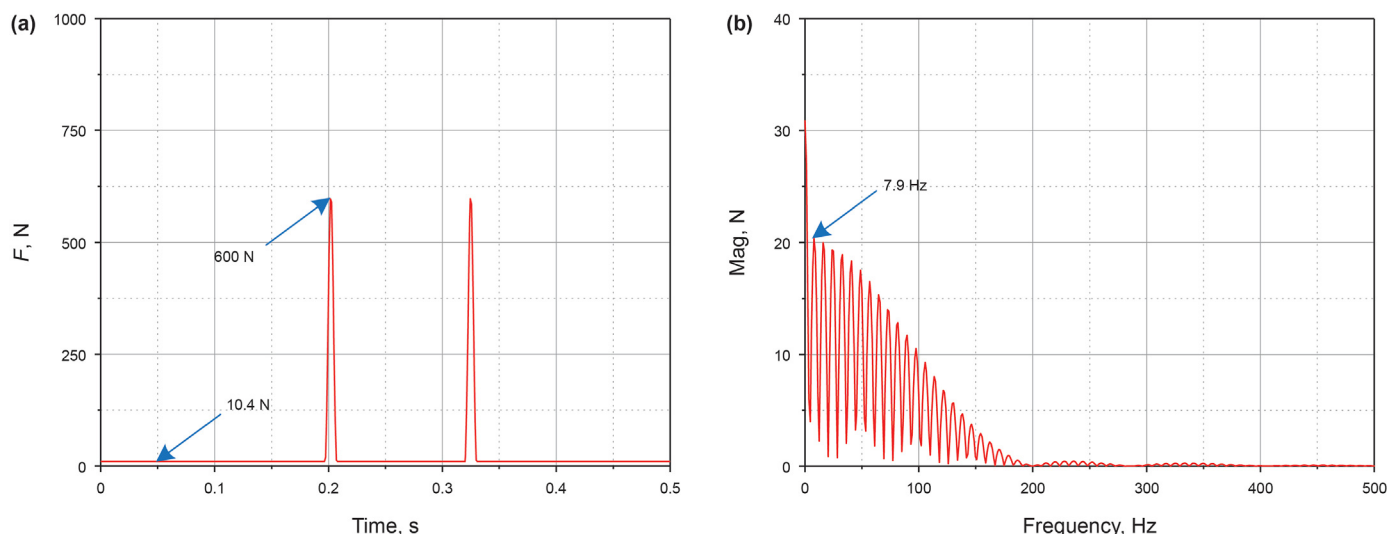

Fig. 5. a The time history curve of the driving force and **b** amplitude spectrum.

Table 3
Comparison of different integration methods.

	I3	SI2	SI1
Solution accuracy	High displacement accuracy	High displacement, velocity and acceleration accuracy	High displacement, velocity, acceleration, and Lagrangian multiplier accuracy
Solving stability	general	good	good
Velocity of solution	fast	slow	slow

Table 4
Comparison of different solver performance.

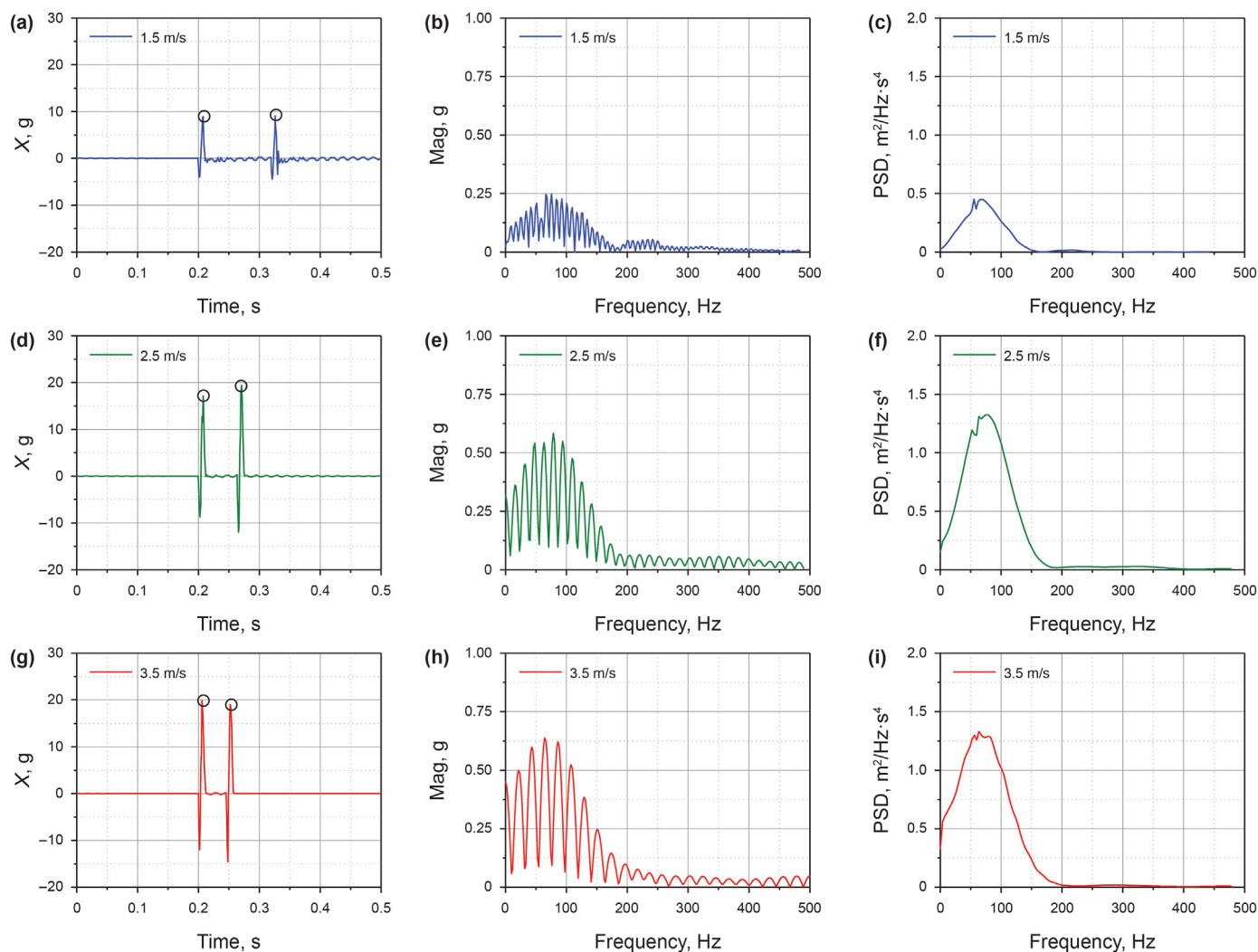|	Gstiff	Wstiff	Dstiff
Algorithm type	Fixed coefficient	Variable coefficient	Variable coefficient
Integral format	I3、SI2、SI1	I3、SI2、SI1	I3
Estimation method	Taylor series	NDF	NDF
Whether the step size produces an error	yes	no	no
Velocity of solution	fast	slow	slow

Fig. 6. Time-frequency responses of the center of mass axial acceleration at different motion velocities: Center of mass axial acceleration **a** time history curve, **b** amplitude spectrum and **c** power spectrum at a velocity of 1.5 m/s; **d** time history curve, **e** amplitude spectrum and **f** power spectrum at a velocity of 2.5 m/s; **g** time history curve, **h** amplitude spectrum and **i** power spectrum at a velocity of 3.5 m/s.

Fig. 6c. The vibration energy is mainly concentrated in the range of 0–100 Hz. The maximum power value is 0.45 m²/Hz·s⁴, and the peak frequency is 55.31 Hz.

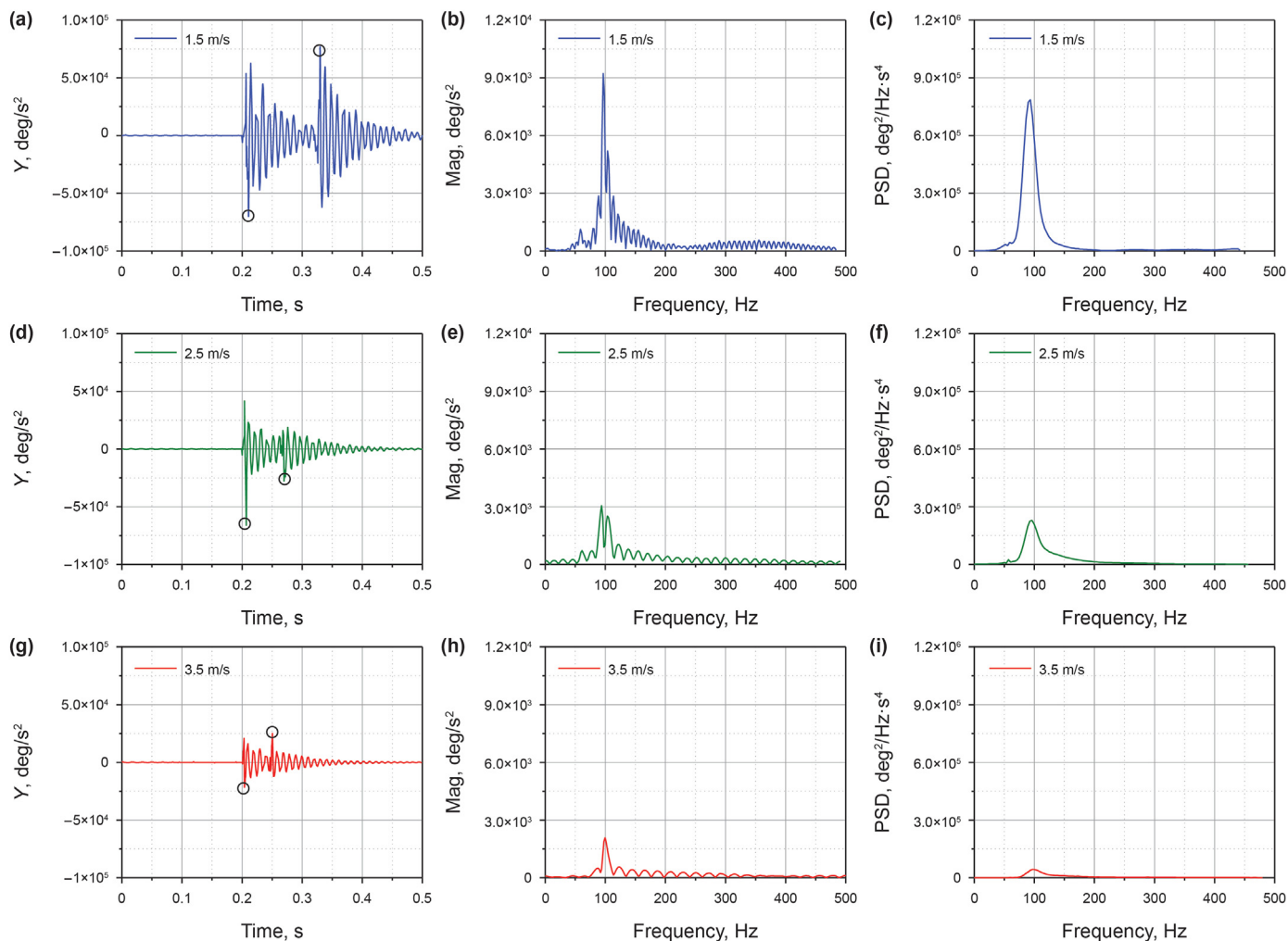As shown in Fig. 6a, d and g, the maximum axial acceleration

Fig. 7. Time-frequency responses of the center of mass pitch acceleration around the *y*-axis at different motion velocities: Center of mass pitch acceleration **a** time history curve, **b** amplitude spectrum and **c** power spectrum at a velocity of 1.5 m/s; **d** time history curve, **e** amplitude spectrum and **f** power spectrum at a velocity of 2.5 m/s; **g** time history curve, **h** amplitude spectrum and **i** power spectrum at a velocity of 3.5 m/s.

amplitude is 9.09 g, 19.63 g and 20.06 g, which indicate that the faster the axial acceleration amplitude of the PIG as it passes through the girth weld increases in conjunction with accelerated motion velocity. Comparing Fig. 6b, e and h suggest that the amplitude of the axial acceleration amplitude spectrum increases as the motion velocity accelerates. As shown in Fig. 6c, f and i, the faster the motion velocity, the larger the power spectrum amplitude.

(2) The dynamic response of the PIG around the *y*-axis

The time history curve of the center of mass pitch acceleration at a motion velocity of 1.5 m/s is shown in Fig. 7a. When the front sealing disc is in contact with the girth weld, the pitch acceleration increases instantaneously, and the PIG posture exhibited a forward trend. Since the upper edge of the front sealing disc initially deviates from the girth weld, the lower axial and radial springs are further compressed. When the lower edge of the sealing disc also deviates from the girth weld, the elastic potential energy of the axial and radial springs is released, and the *y*-axis pitch acceleration is reduced to a minimum value of 7.01 × 10⁴ deg/s² under the positive moment. After the front sealing disc passes through the girth weld, the pitching vibration gradually attenuates under the

damping of the system. When the rear sealing disc is in contact with the girth weld, the pitch acceleration displays a sudden decrease. When the rear sealing disc deviates from the weld, the peak value of the pitch acceleration is 7.68 × 10⁴ deg/s². The amplitude spectrum of the center of mass pitch acceleration at a motion velocity of 1.5 m/s is shown in Fig. 7b. The maximum amplitude is 9.21 × 10³ deg/s², the peak frequency is 96.43 Hz, and the main distribution interval is 79.41–122.90 Hz. The power spectrum of the center of mass pitch acceleration at a motion velocity of 1.5 m/s is shown in Fig. 7c. The maximum power value is 7.86 × 10⁵ deg²/Hz·s⁴, the peak frequency is 93.32 Hz, and the energy is mainly distributed between 76.04 Hz and 120.97 Hz.

As shown in Fig. 7d and g, the vibration pattern of the *y*-axis pitch acceleration caused by the PIG model passing through the girth at 2.5 m/s and 3.5 m/s is similar to 1.5 m/s. Regarding amplitude, the pitch acceleration displays a gradual decline as the motion velocity increases. Comparing Fig. 7b, e and h indicate a decrease in the amplitude of the pitch-acceleration amplitude spectrum and excited harmonic components when the motion velocity accelerates. As illustrated by Fig. 7c, f and i, a faster the motion velocity, induces a smaller pitch acceleration power value, and the primary energy distribution band is narrows gradually.
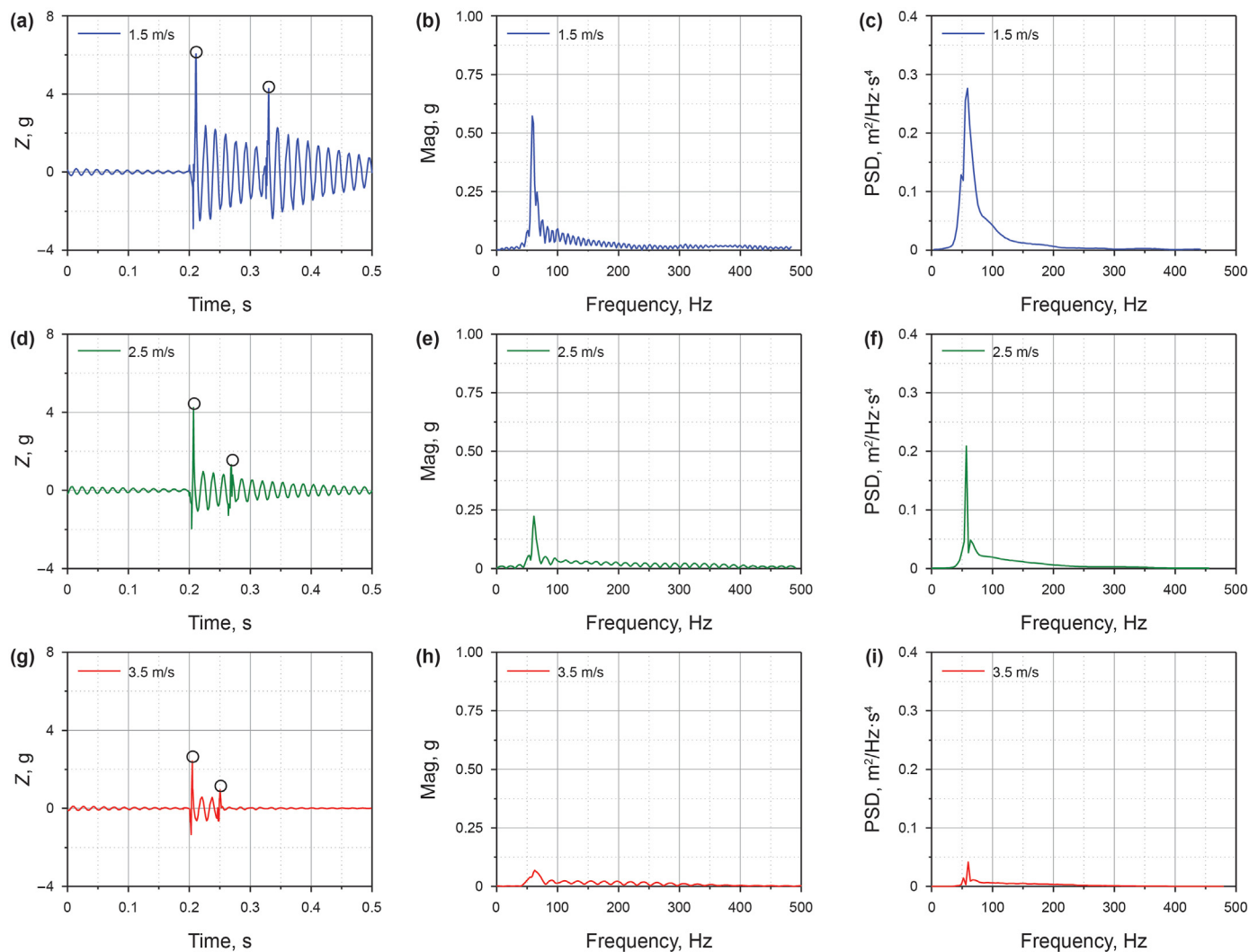
Fig. 8. Time-frequency responses of the vertical acceleration of the center of mass at different motion velocities: Center of mass vertical acceleration **a** time history curve, **b** amplitude spectrum and **c** power spectrum at a velocity of 1.5 m/s; **d** time history curve, **e** amplitude spectrum and **f** power spectrum at a velocity of 2.5 m/s; **g** time history curve, **h** amplitude spectrum and **i** power spectrum at a velocity of 3.5 m/s.

(3) Dynamic response in the radial direction of the pipeline

The time history curve of the z-axis vertical acceleration at a motion velocity of 1.5 m/s is shown in Fig. 8a. When the front sealing disc is in contact with the girth weld, the vertical acceleration of the center of mass is rapidly reduced. Since the PIG exhibited a forward tendency during the entire process, the upper edge of the front sealing disc is the first to deviate from the girth weld, and the radial spring positioned at the lower end is further compressed. After the front sealing disc completely passes through the girth weld, the potential energy of the axial and radial springs is released, and the vertical acceleration of the PIG is rapidly increased to a maximum value of 6.06 g. The maximum vertical acceleration caused by the rear sealing disc passing through the girth weld is 4.27 g, which is significantly smaller than the previous value, indicating a weak vertical vibration as a result. The amplitude spectrum of the z-axis vertical acceleration at a motion velocity of 1.5 m/s shown in Fig. 8b indicates that the amplitude-frequency curve exhibited a distinct peak with a maximum amplitude of 0.57 g, and a peak frequency of 58.62 Hz, which is close to the sixth-order natural frequency of the model. The power spectrum of the z-axis vertical acceleration at a motion velocity of 1.5 m/s is shown in

Fig. 8c. The power spectrum displays a visible peak, the maximum power is 0.28 $m^2/Hz \cdot s^4$, and the peak frequency is 58.76 Hz, while the energy is mainly distributed between 38.02 Hz and 124.43 Hz.

Fig. 8d and g suggest that the vertical vibrations caused by the PIG passing through the girth weld at motion velocities of 2.5 m/s and 3.5 m/s are the same as those at 1.5 m/s. It is evident that a faster the motion velocity produces smaller vertical acceleration amplitude, the shorter the time required to pass the girth weld, and the faster the vertical acceleration decays. Fig. 8b, e and h suggest that the faster motion velocity reduces the amplitude of the amplitude spectrum. It is apparent from Fig. 8c, f and i that as the motion velocity of the PIG increases, the maximum peak value of the vertical acceleration power spectrum gradually decreases, while the energy distribution range also narrows around the center frequency of 45 Hz.

5.2. Dynamic response of the PIG at different center of mass positions

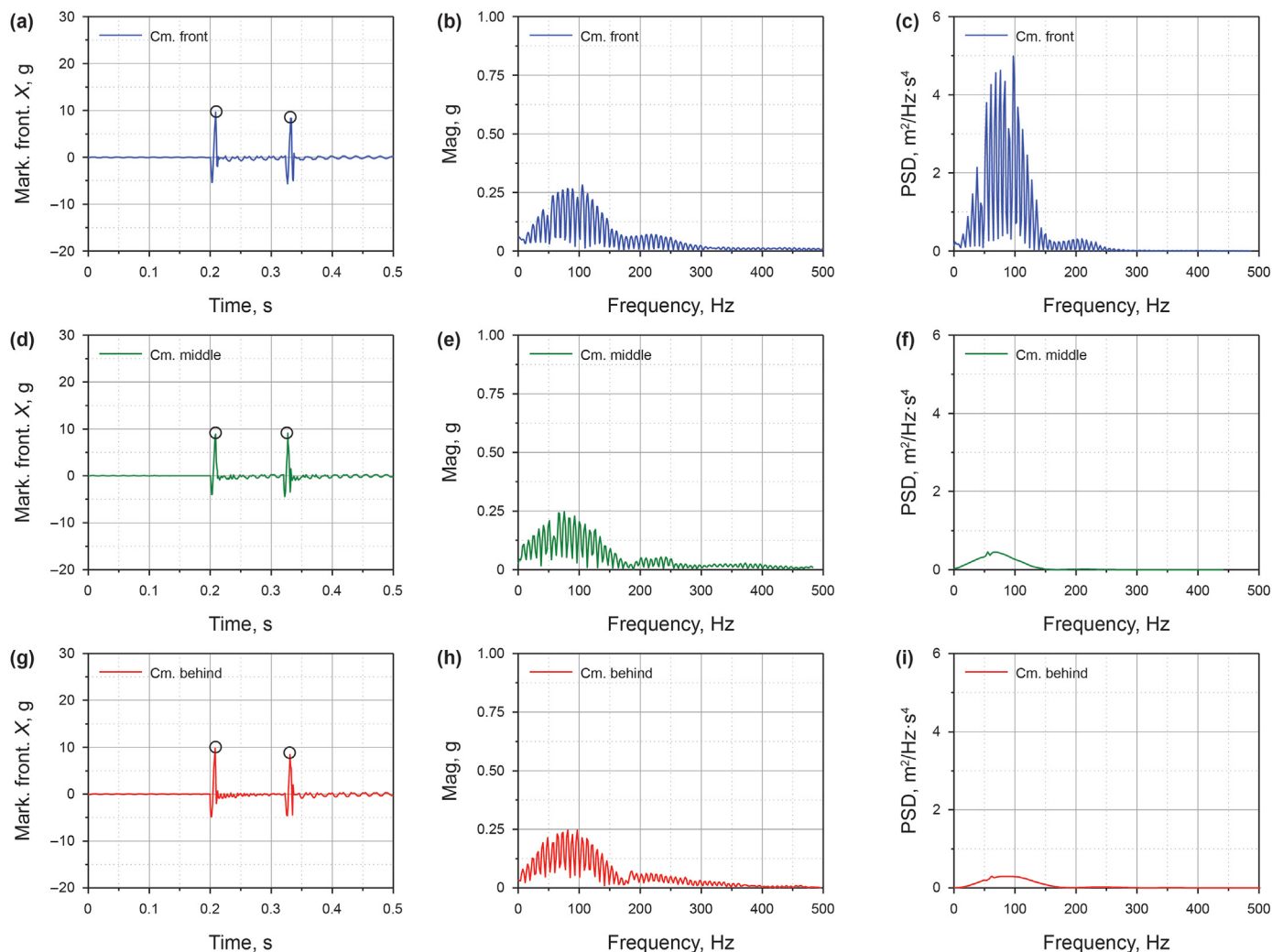(1) Dynamic response in the axial direction of the pipeline

Fig. 9. Time-frequency responses of the front mark point axial acceleration of the different center of mass positions at a velocity of 1.5 m/s: Axial acceleration **a** time history curve, **b** amplitude spectrum and **c** power spectrum when the center of mass is located in the front; **d** time history curve, **e** amplitude spectrum and **f** power spectrum when the center of mass is located in the middle; **g** time history curve, **h** amplitude spectrum and **i** power spectrum when the center of mass is located in the rear.

For the rigid body of a PIG, the axial motion state of each point is the same. Therefore, the front mark point is used to indicate the state of the axial acceleration when the center of mass position changes.

Fig. 9a indicates the time history curve representing the axial acceleration of the front mark point when the PIG's center of mass is located in the front. The axial acceleration amplitude spectrum of the front mark point is shown in Fig. 9b, while Fig. 9c illustrates its axial acceleration power spectrum. Fig. 9a, d and g indicate that when the center of mass position is different, the vibration peaks caused by the sealing disc passing through the girth weld are extremely close together. As shown in Fig. 9b, e and h, the various spectrograms at different center of mass positions are approximately the same. It is apparent from Fig. 9c, f and i that the power peak reaches its maximum level when the center of mass is located in the front and more harmonic components are excited. When the center of mass is located in the middle and the back, the shape of the power spectrum curve remains the same.

(2) The dynamic response of the PIG around the *y*-axis

For the rigid body of a PIG, the rotation state of each point

around the *y*-axis is the same. Therefore, the front mark point is used to indicate the state of the pitch acceleration when the center of mass position changes. Fig. 10a illustrates the time history curve referencing the pitch acceleration of the front mark point when the PIG's center of mass is located in the front. Two distinct pulse peaks are evident, and the amplitudes are 2.47×10^4 deg/s^2 and 2.86×10^4 deg/s^2. The amplitude spectrum referring to the pitch acceleration of the front mark point is shown in Fig. 10b. The first peak frequency is 50.22 Hz, and the amplitude is 2.53×10^3 deg/s^2; the second peak frequency is 94.29 Hz, and the amplitude is 1.63×10^3 deg/s^2. The power spectrum referencing the pitch acceleration of the front mark point is shown in Fig. 10c. Two significant peaks are evident, the first peak frequency is 47.63 Hz, with a corresponding amplitude of 4.68×10^6 deg^2/Hz·s^4; the second peak frequency is 89.54 Hz, with a corresponding amplitude of 1.95×10^6 deg^2/Hz·s^4.

From Fig. 10a, d, and g, it is apparent that the PIG pitch acceleration curve is significantly different when the center of mass changes. When the center of mass is located in the front, the pitch vibration caused by the sealing disc passing through the girth weld is weak. When the center of mass is located in the middle, two obvious pulse peaks are evident in conjunction with apparent
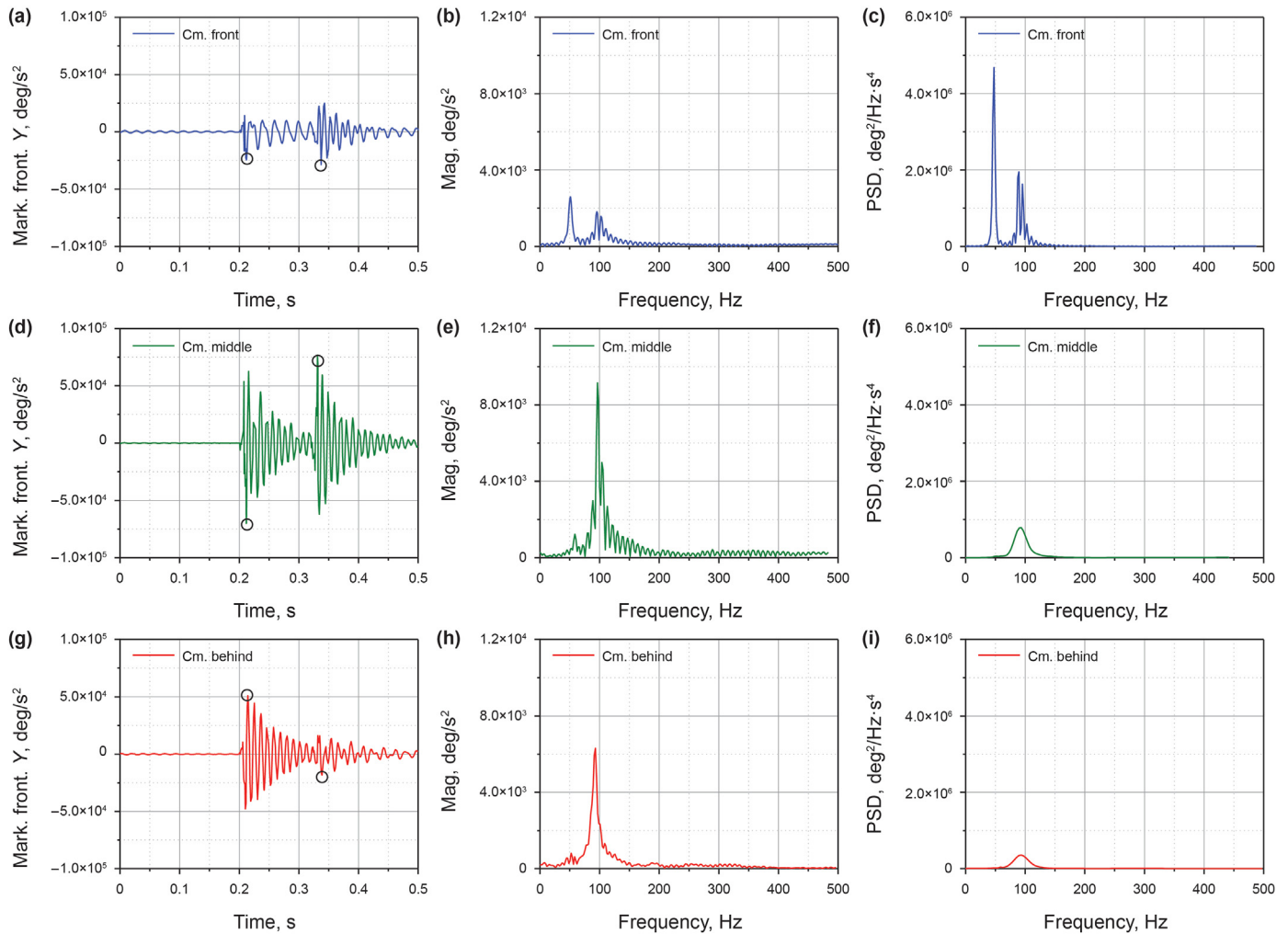
Fig. 10. Time-frequency responses of the front mark point pitch acceleration of the different center of mass positions at a velocity of 1.5 m/s: Pitch acceleration **a** time history curve, **b** amplitude spectrum and **c** power spectrum when the center of mass is located in the front; **d** time history curve, **e** amplitude spectrum and **f** power spectrum when the center of mass is located in the middle; **g** time history curve, **h** amplitude spectrum and **i** power spectrum when the center of mass is located in the rear.

attenuation trends. Examination of Fig. 10b, e and h suggest that when the center of mass is located in the middle, the amplitude spectrum range referring to the pitch acceleration is the largest. As shown in Fig. 10f and i, the range of the power spectrum referring to pitch acceleration is significantly reduced when the center of mass is located in the middle and rear.

(3) Dynamic response in the radial direction of the pipeline

When the position of the center of mass changes, the front mark point is also used to indicate the state of the vertical acceleration. Fig. 11a indicates the time history curve referring to the vertical acceleration of the front mark point when the PIG's center of mass is located in the front. A significant pulse peak is visible, corresponding to an amplitude of 6.92 g, which is caused by the front sealing disc passing through the girth weld. This maximum peak is followed by the vertical acceleration which is reduced when exposed to damping action. However, it is unclear from the image when the rear sealing disc passes the girth weld. The Fig. 11b denotes the amplitude spectrum of the vertical acceleration of the front mark point. The maximum amplitude is 0.65 g and the frequency is 51.24 Hz. The vertical acceleration power spectrum of the front mark point is shown in Fig. 11c. The maximum power value is

16.02 m^2/Hz·s^4 and the frequency is 92.51 Hz.

When the center of mass is located in the middle, the acceleration pulse change caused by the sealing disc passing through the girth weld is clearly visible as illustrated in Fig. 11a, d, and g. When the center of mass located in the rear, the vibration caused by the front sealing disc passing through the girth weld is significantly larger than that of the rear sealing disc. As shown in Fig. 11e and f, when the center of mass is located in the middle and rear, two distinct peaks can be observed in the vertical acceleration spectrum of the PIG. Fig. 11f and i shows that when the center of mass is located in the middle and rear, the maximum power value of the vertical acceleration power spectrum of the PIG's front end is significantly reduced.

6. Conclusions

(1) Combined with the dynamic model of the multi-system pipeline robot system established by the theoretical model of the sealing disc dynamics, the movement characteristics of the PIG are comprehensively considered. When the PIG passes through the girth weld at different velocities, obvious collision vibration will occur. The center of mass curves of the axial, vertical and pitch accelerations can all exhibit abrupt,
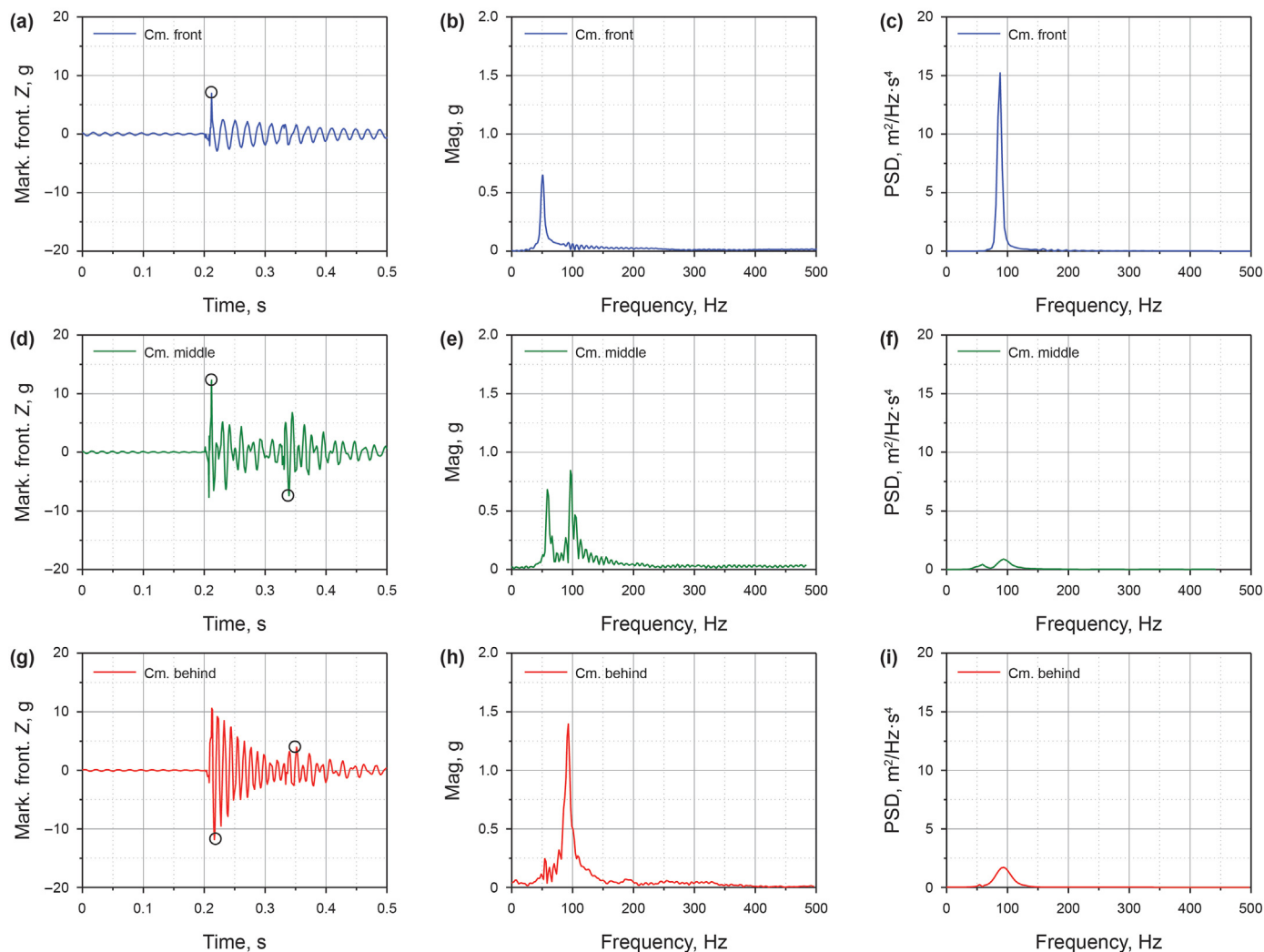
Fig. 11. Time-frequency responses of the front mark point vertical acceleration of the different center of mass positions at a velocity of 1.5 m/s: Vertical acceleration **a** time history curve, **b** amplitude spectrum and **c** power spectrum when the center of mass is located in the front; **d** time history curve, **e** amplitude spectrum and **f** power spectrum when the center of mass is located in the middle; **g** time history curve, **h** amplitude spectrum and **i** power spectrum when the center of mass is located in the rear.

pulse-type changes that are most severe when occurring during axial acceleration. Furthermore, the acceleration peak generated by the front sealing disc passing through the girth weld is larger in the vertical and pitch accelerations. After the model passes the girth weld, the decay rate of the axial acceleration is faster than the vertical and pitch acceleration decay velocities.

(2) A frequency analysis of the axial, pitch and vertical accelerations of the PIG indicated that the main frequency components of the amplitude spectrum are concentrated in the range of 0–200 Hz, while the primary frequency components of the power spectrum are concentrated in the range of 0–150 Hz. The maximum peak frequency remains consistent at about 73 Hz, while faster motion velocity causes less harmonic components to be excited. The vertical and pitch acceleration vibrations significantly weakens as the motion velocity increases. The amplitude and power peaks exhibit a substantial reduction, while the distribution range of the vibration energy narrows considerably.

(3) Changes in the PIG's center of mass positions have little effect on its axial vibration, while the pitch and vertical vibration conditions are significantly different due to these

modifications. When the center of mass is located in the front, the axial, pitch and vertical vibration appear to be the weakest. When the center of mass is located in the middle, the pitch vibration is the most obvious. When the center of mass is located in the rear, the vertical vibration of the front part of the PIG is the most intense.

The results can contribute to optimizing the design of the PIG's structure, extending the service cycle, and improving the efficiency of the internal inspection operation.

Acknowledgements

References

Aksenov, D.V., Shcherbakov, V.I., Leshchenko, V.V., 2012. Self-oscillation of flaw-

detection equipment for arterial gas pipelines. CHEM PET ENG 48 (6), 364—371. https://doi.org/10.1007/s10556-012-9625-0.

Aksenov, D.V., Shcherbakov, V.I., Leshchenko, V.V., 2013. Selection of structural parameters of an inspection pig for arterial oil and gas pipelines from conditions of dynamics. CHEM PET ENG 49 (4), 265—269. https://doi.org/10.1007/s10556-013-9738-0.

Esmaeilzadeh, F., Mowla, D., Asemani, M., 2009. Mathematical modeling and simulation of pigging operation in gas and liquid pipelines. J. Petrol. Sci. Eng. 69 (1), 100—106. https://doi.org/10.1016/j.petrol.2009.08.006.

Fótos, R., Koncsik, Z., Lukács, J., 2012. Application of risk-informed inspection strategy to improve the lifetime and efficiency of cleaning pigs. Mater. Sci. Forum 729, 338—343. 10.4028/www.scientific.net/msf.729.338.

Hendrix, M.H.W., Liang, X., Breugem, W.P., et al., 2017a. Characterization of the pressure loss coefficient using a building block approach with application to bypass pigs. J. Petrol. Sci. Eng. 150, 13—21. https://doi.org/10.1016/j.petrol.2016.11.009.

Hendrix, M.H.W., Ijsseldijk, H.P., Breugem, W.P., et al., 2017b. Development of velocity controlled pigging for low pressure pipelines. In: Proceedings of the 18th International Conference on Multiphase Production Technology, 7-9 June. Cannes. France5.

Hu, X.W., Zhou, C.F., Duan, M.L., et al., 2014. Reliability analysis of marine risers with narrow and long corrosion defects under combined loads. Petrol. Sci. 11, 139—146. https://doi.org/10.1007/s12182-014-0325-6.

Liang, Z., He, H.G., Cai, W.L., 2017. Velocity simulation of bypass hole PIG with a brake unit in liquid pipe. J. Nat. Gas Sci. Eng. 42, 40—47. https://doi.org/10.1016/j.jn-gse.2017.03.011.

Mcdonald, A.E., Baker, O., 1964. Multiphase flow in pipelines. Oil Gas J. 62 (27), 118—119.

Mirshamsi, M., Rafeeyan, M., 2012. Speed control of pipeline pig using the QFT method. Oil Gas Sci. Technol. 67 (4), 693—701. https://doi.org/10.2516/ogst/2012008.

Mirshamsi, M., Rafeeyan, M., 2015a. Dynamic analysis and simulation of long pig in gas pipeline. J. Nat. Gas Sci. Eng. 23 (3), 294—303. https://doi.org/10.1016/j.jngse.2015.02.004.

Mirshamsi, M., Rafeeyan, M., 2015b. Dynamic analysis of pig through two and three-dimensional gas pipeline. J. Appl. Fluid Mech. 8 (1), 43—54. https://doi.org/10.36884/jafm.8.01.21406.

Nguyen, T.T., Kim, D.K., Rho, Y.W., et al., 2001a. Dynamic modeling and its analysis for PIG flow through curved section in natural gas pipeline. Computational Intelligence in Robotics and Automation, 2001. Proceedings 2001 IEEE International Symposium on IEEE 4, 492—497. https://doi.org/10.1109/cira.2001.1013250.

Nguyen TT, Yoo HR, Rho YW, et al. Velocity control of PIG using bypass flow in natural gas pipeline. Industrial Electronics, 2001. Proceedings. ISIE 2001. IEEE International Symposium on. IEEE, 2001;2:863-868. https://doi.org/10.1007/bf03185671.

Nguyen, T.T., Kim, S.B., Yoo, H.R., et al., 2001c. Modeling and simulation for pig with bypass flow control in natural gas pipeline. KSME Int. J. 15 (9), 1302—1310. https://doi.org/10.1007/BF03185671.

Niechele, A.O., Braga, A.M.B., Aevedo, L.F.A., 2000. Transient Pig Motion through Non-isotherm-al Gas and Liquid Pipelines. Proceedings of the 2000 International Pipeline Conference. 1–5 October. Canada, Calgary, Alberta. https://doi.org/10.1115/ipc2000-175.

Patricio, R.A.C., Baptista, R.M., Rachid, F.B.D.F., et al., 2020. Numerical simulation of pig motion in gas and liquid pipelines using the Flux-Corrected Transport method. J. Petrol. Sci. Eng. 189, 106970. https://doi.org/10.1016/j.petrol.2020.106970.

Quarini, J., Shire, S., 2007. A review of fluid-driven pipeline pigs and their applications. P I MECH ENG E-J PRO. 221 (1), 1—10. https://doi.org/10.1243/0954408JPME108.

Ren, H.X., Shi, D.Y., Xu, Y., et al., 2017. Research on dynamics and vibration response in pipeline inspection Gauge (PIG) based on the CEL method. INTER-NOISE and NOISE-CON congress and conference proceedings, 255. Institute of Noise Control Engineering, pp. 56—67, 7.

Shi, Y., Zhang, C., Li, R., et al., 2015. Theory and application of magnetic flux leakage pipeline detection. Sensors 15 (12), 31036—31055. https://doi.org/10.3390/s151229845.

Shi, D.Y., Xu, Y., Wasim, M.K.H., et al., 2017. Fluid-solid Coupling Numerical Analysis of Dynamic Vibration Characteristics of the Pipeline Inspection Gauge (PIG) in the Pipeline. INTER-NOISE and NOISE-CON Congress and Conference Proceedings, vol. 255. Institute of Noise Control Engineering, pp. 261—269.

Tolmasquim, S.T., Nieckele, A.O., 2008. Design and control of pig operations through pipelines. J. Petrol. Sci. Eng. 62 (3-4), 102—110. https://doi.org/10.1016/j.petrol.2008.07.002.

Xie, M.J., Tian, Z.G., 2018. A review on pipeline integrity management utilizing inline inspection data. Eng. Fail. Anal. 92, 222—239. https://doi.org/10.1016/j.engfailanal.2018.05.010.

Xu, X.X., Gong, J., 2005. Pigging simulation for horizontal gas-condensate pipelines with low liquid loading. J. Petrol. Sci. Eng. 48 (3-4), 272—280. https://doi.org/10.1016/j.petrol.2005.06.005.

Yan, Y.M., Liang, Y.T., Zhang, H.R., et al., 2019. A two-stage optimization method for unmanned aerial vehicle inspection of an oil and gas pipeline network. Petrol. Sci. 16, 458—468. https://doi.org/10.1007/s12182-019-0305-y.

Yu, T., Li, C.X., Yao, B., et al., 2020. Standard friction prediction model of long-distance hot oil pipelines. Petrol. Sci. 17, 487—498. https://doi.org/10.1007/s12182-019-00417-w.

Zhang, H., Zhang, S.M., Liu, S.H., et al., 2015a. Chatter vibration phenomenon of pipeline inspection gauges (PIGs) in natural gas pipeline. J. Nat. Gas Sci. Eng. 27 (11), 1129—1140. https://doi.org/10.1016/j.jngse.2015.09.054.

Zhang, H., Zhang, S.M., Liu, S.H., et al., 2015b. Measurement and analysis of friction and dynamic characteristics of PIG's sealing disc passing through girth weld in oil and gas pipeline. Measurement 64 (3), 112—122. https://doi.org/10.1016/j.measurement.20-14.12.046.

Zhang, H., Dong, J.H., Cui, C., Liu, S.H., 2020. Stress and strain analysis of spherical sealing cups of fluid-driven pipeline robot in dented oil and gas pipeline. Eng. Fail. Anal. 108, 104294. https://doi.org/10.1016/j.engfailanal.2019.104294.

Zhao, G.H., Liang, Z., Zhao, H.R., et al., 2013. Failure analysis of high-drop pipeline in the process of dewatering. Eng. Fail. Anal. 33, 139—150. https://doi.org/10.1016/j.engf-ailanal.2013.04.019.

Zhu, X.X., Zhang, S.M., Li, X.L., et al., 2015. Numerical simulation of contact force on bi-directional pig in gas pipeline: at the early stage of pigging. J. Nat. Gas Sci. Eng. 23, 127—138. https://doi.org/10.1016/j.jngse.2015.01.034.